JOURNAL OF AIRCRAFT
Vol. 43, No. 6, November–December 2006

Frequency Response Model for Branched Pneumatic Sensing Systems

Stephen A. Whitmore*
Utah State University, Logan, Utah 84322-4130

DOI: 10.2514/1.20759

A frequency response model for branched pneumatic sensors is developed. A typical application is prediction of pneumatic latency and attenuation in aircraft airdata systems, where pneumatic lines are branched to feed a variety of instruments, navigation systems, and pilot displays. The model is developed using small perturbations of the unsteady Navier–Stokes equations. The linearized equations are radially averaged and expressed in the frequency domain. The result is one-dimensional boundary value problem where the pressure oscillation for a given frequency is expressed as a function of position within the sensor. Assuming constant tube geometry and gas properties along an arbitrarily small tubing element allows a closed-form solution of the boundary value equations. This solution becomes a fundamental building block for solving the frequency response of more complex pneumatic geometries. The analysis process employed is similar to applying Kirchhoff's laws to analyze complex electrical circuits. The model predictions are compared against experimental data generated for a simple two-branch configuration. Comparisons for both symmetrical and unbalanced branches are presented. Experiment setup and procedures are described. The comparisons show that the model accurately predicts both the magnitude and phase frequency response of dominant and reflected wave harmonics within each branch of the system.

Nomenclature

A_c	=	cross-sectional tube area, cm^2
$A(\omega)$	=	constant of integration (1)
$B(\omega)$	=	constant of integration (2)
C_p	=	specific heat at constant pressure, $kJ/kg \cdot K$
c	=	sonic velocity, m/s
D	=	tube diameter, cm
f_0	=	fundamental frequency, Hz
i	=	frequency, node index, iteration index
J_0	=	zeroth-order Bessel function
J_1	=	first-order Bessel function
J_2	=	second-order Bessel function
j	=	imaginary constant, $(-1)^{1/2}$, iteration index
K	=	proportionality constant for polytropic process
L	=	tube length, cm
m	=	main node index
N_h	=	number of harmonics in excitation signal
n	=	node number
P	=	general pressure term, kPa
$P_L(\omega)$	=	sensed pressure for given input frequency, kPa
$P_0(\omega)$	=	surface pressure input for given input frequency, kPa
$P(x, \omega)$	=	pressure in tube at position x for given input frequency, kPa
Pr	=	Prandtl number
R	=	tube radius, cm
R_g	=	gas constant, $kJ/kg \cdot K$
r	=	radial coordinate, cm
T	=	temperature, K
t	=	time, s
U	=	flow velocity, m/s
V	=	sensor volume, cm^3
V_m	=	main node volume, cm^3
Ve	=	effective sensor volume including downstream impedance, cm^3
x	=	longitudinal coordinate, cm
α	=	shear wave number
Γ_p	=	wave propagation factor
γ	=	ratio of specific heats at constant pressure and volume, $kJ/kg \cdot K$
δf	=	frequency increment, Hz.
κ	=	thermal conductivity, $N/s \cdot K$
μ	=	dynamic viscosity, $N \cdot s/m^2$
ξ	=	polytropic exponent
ρ	=	general density term, kg/m^3
ρ_0	=	mean density in tube section, kg/m^3
Φ	=	impedance of parallel branch downstream of main node
ω	=	angular frequency of input pressure, rad/s
1	=	frequency response test branch 1 subscript
2	=	frequency response test branch 2 subscript

I. Introduction

MODERN aircraft are becoming increasingly more complex and rely on flight computers to manage onboard systems, increase safety and efficiency, and reduce pilot workloads. One of the key components of modern avionics is the airdata system where pressure measurements are converted to a variety of parameters such as airspeed, altitude, sink rate, and dynamic pressure. These parameters are used directly by the pilot to fly the airplane and are also used by avionics computers for vehicle navigation tasks. The pneumatic layout of a typical airdata system for a commercial aircraft is shown in Fig. 1. Airdata components of military avionics systems are even more complex with pitot and static pressure sources serving multiple instruments and computer systems through a morass of pneumatic branches, fittings, and connectors. The focus of this paper is on the development and verification of frequency response model for pneumatic systems with one or more parallel branches or components. This model will be directly applicable to the frequency response and measurement latency prediction of the complex pneumatic configurations described in this paragraph.

The primary difficulty with obtaining high-fidelity measurements from pneumatic systems is acoustical distortion due to friction, pneumatic resonance, and wave reflections within the various branches of the pneumatic system. Most of the signal distortion

Received 26 October 2005; revision received 31 March 2006; accepted for publication 9 April 2006.

*Assistant Professor, Mechanical & Aerospace Engineering Department, 4130 Old Main Hill/UMC 4130. Associate Fellow AIAA.

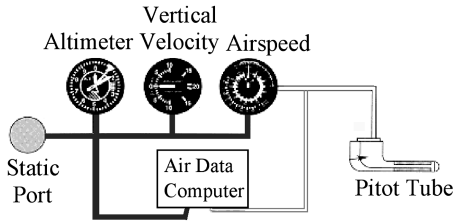

Fig. 1 Typical pneumatic layout of an airdata system for a commercial aircraft.

occurs within the pneumatic tubing used to "plumb" the components of the system. To avoid pneumatic distortion, experiment designers ideally would mount the pressure sensor at or very near the desired surface measurement location. In some cases, this technique offers a viable solution; unfortunately, for many applications, as with the airdata system components, in situ mounting is impractical and pneumatic distortion is an inherent part of the system design.

For these and other reasons, the problems associated with predicting tube flow dynamics has been studied extensively. Rayleigh, Kelvin, and Helmholtz first studied steady pipe flows, and the behavior of organ pipe harmonics in the late 19th century and early 20th century (as cited by Stephens and Bate [1]). Iberall [2] performed the first serious engineering analysis of oscillatory flow in the pressure lines of simple pneumatic measurement configurations. Later Lamb [3] developed a simple time domain model for pneumatic systems. Unlike the model developed by Iberall that mandated sinusoidal inputs to the system, Lamb's model was accurate at predicting sensor rise times for discrete ramp and step inputs. Building on the model developed by Iberall, Schuder and Binder [4] and Hougen et al. [5] collectively developed a closed-form model for the frequency response of simple tubing geometries with constant wall temperature. The model of [4,5] was applied to the prediction of the response of systems with arbitrary inputs. Later Berg and Tijdeman [6] extended the models of [4,5] to complex geometries consisting of flow paths with serially installed cascades of tubes and volumes. The methods of [6] are currently considered the state-of-the-art for the calculation of pneumatic responses for cascaded geometries with constant wall temperatures and continuum flow. Tijdeman [7] presents a succinct summary of existing tube response theories, the assumptions allowed in their derivations, and their limits of applicability. Parrot and Zorumski [8] investigated the dynamic transmission of sound in a glass tube subjected to very large temperature gradients in 1990. Whitmore et al. [9,10] and Whitmore [11] extended the work of [6,7] to model the frequency response of cascaded pneumatic systems with temperature gradients and rarified flow conditions. Data presented by [8] were used in part to validate the model presented in [9–11].

None of the models developed by these references are valid for multiple-branch systems. In contrast to a *cascaded pneumatic system* that has a single flow path with constant mass flow throughout, a system with multiple line branches splits the mass flow amongst the sensor branches. The total mass flow in all branches must equal the incoming mass flow at the surface pressure port. An example of a cascaded system is a pressure line with pressure fittings or pipes of different diameters joined by a coupler. An example of a *branched pneumatic system* is the aircraft cockpit instrumentation depicted in Fig. 1. Cascaded pneumatic systems are analogous to serial electrical circuits, and branched pneumatic systems are analogous to parallel pneumatic circuits. In keeping with the electrical systems analogy, this paper will refer to cascaded pneumatic components as *serial*, and branched components as *parallel*. To date, no good analytical model has been developed for multiple-branch systems.

II. Presentation of the Boundary Value Equations

The discussion to be presented in this section is based on acoustical theories developed to analyze the dynamic responses of pneumatic systems that are subjected to *purely sinusoidal pressure inputs*. The *transfer-functions* to be developed can be applied to arbitrary pressure inputs by first transforming the input signal to the frequency domain using a numerical Fourier transform, convolving the resulting spectrum with the pressure response transfer function, and then inverse transforming the resulting spectrum to the time domain. By applying these analysis methods to an installed aircraft system, the calculated transfer functions can be used for real-time attenuation and latency compensation using previously published spectral deconvolution methods [12]. Doebelin [13] presents an excellent introduction to the methods used to analyze the frequency response of acoustical systems.

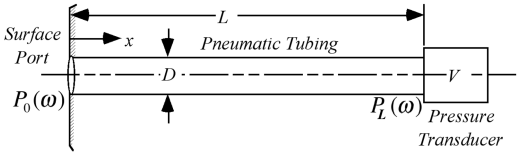

Fig. 2 Schematic of idealized pressure sensor configuration.

In this section boundary value equations are presented first. These boundary value equations are solved in the frequency domain to give a closed-form solution for a tube with constant cross section, temperature, and gas properties. The analytical solution is used as a building block for more complex solutions where the wall temperature distribution, fluid properties, and tube geometries are allowed to vary in arbitrary manners. The simple (*fundamental*) sensor configuration is pictured in Fig. 2. The configuration is modeled as a straight cylindrical tube with a dimensionless (*no length*) volume V, representing the internal volume of the pressure transducer attached to the downstream end. A longitudinal coordinate x is defined as positive moving aft from the upstream (*port*) end of the tube. The cross-sectional area of the tube is assumed to be constant. Unsteady surface pressure impulses $P_0(\omega)$, with angular frequency ω, propagate as longitudinal waves down the tube and are sensed by the pressure transducer as $P_L(\omega)$.

The dynamic response model for the configuration depicted in Fig. 2 is derived from the unsteady Navier–Stokes equations expressed in cylindrical coordinates and linearized using small perturbation theory. The energy equation is decoupled from the equations of momentum and continuity, by assuming that the longitudinal wave expansion within the tube is a polytropic process [2,6–11]. In a polytropic process the relationship between density and pressure is independent of temperature, and is described by the simple model

$$P = K\rho^{\xi} \tag{1}$$

In Eq. (1), K is a constant of proportionality, and ξ is the "polytropic exponent" that accounts for the transfer of energy between the wall and the mean flow. Because of the time phasing differences between the energy and momentum equations, ξ is generally a complex number. In two special cases, *isothermal flow and isentropic flow*, ξ is a real number with $\xi = 1.0$ corresponding to an isothermal process and $\xi = \gamma$ corresponding to an isentropic process. The parameter γ is ratio of specific heats at constant pressure and constant volume.

The momentum equation is integrated across the tube cross section to give the radially averaged mean local flow velocity in terms of the longitudinal pressure gradient. The resulting momentum equation is coupled with the radially averaged continuity equation with the result being a wave equation that describes the pressure propagation in the tube. When the linearized boundary value equations are represented in the frequency domain, the partial differential equation describing wave motion in the time domain becomes an ordinary differential equation whose coefficients are functions of input pressure frequency. The resulting frequency domain model is

$$\frac{\mathrm{d}^2 P(x,\omega)}{\mathrm{d}x^2} = \left(\omega \frac{\Gamma_p}{c}\right)^2 P(x,\omega) \tag{2}$$

The pressure term in Eq. (2), $P(x,\omega)$, is the tubing pressure at an arbitrary position (x) in the tube, and is also a function of the angular

frequency of the input sinusoid. The downstream boundary condition at $x = L$ is

$$\frac{\mathrm{d}P(L,\omega)}{\mathrm{d}x} = -\left(\omega\frac{\Gamma_p}{c}\right)^2\frac{V}{A_c}P(L,\omega) \tag{3}$$

The pressure at the upstream boundary ($x = 0$) is the prescribed pressure input $P_0(\omega)$. At any longitudinal position (x) the radially averaged fluid velocity is

$$U(x,\omega) = \frac{[\mathrm{d}P(x,\omega)]/\mathrm{d}x}{j\omega(\xi/\gamma)\Gamma_p^2\rho_0} \tag{4}$$

In the acoustical theories used to analyze this configuration, the tubing diameter is considered to be small compared to the tube length, and the resulting flow velocities are small. Consequently, the flow is quasi-incompressible and ρ_o can be assumed to be constant along the length of the tube. Depending on the detail and methods employed in the decoupling of the energy equation, Γ_p will have one of several forms. Tijdeman [7] presents an excellent survey of the propagation factors published in the open literature. For continuum flow conditions the formula for Γ_p considered most accurate [7,9–11] is

$$\Gamma_p = \sqrt{\frac{\gamma J_0(\alpha)}{\xi J_2(\alpha)}} \tag{5}$$

In Eq. (5) parameter, α is the shear wave number given by

$$\alpha = \frac{j^{3/2}}{2}\sqrt{\frac{\omega\rho_0 D^2}{\mu}} \tag{6}$$

In Eq. (6) the parameter μ is the dynamic viscosity of the working fluid, and J_0, J_2 are zeroth- and second-order Bessel functions of the first kind. The variation of ξ with the shear wave number is given by

$$\xi = \frac{1}{1 + [(\gamma-1)/\gamma]\{[J_2(\sqrt{Pr}\alpha)]/[J_0(\sqrt{Pr}\alpha)]\}} \tag{7}$$

In Eq. (7), Pr is defined as the ratio of heat capacity to thermal conductivity ($\mu C_p/\kappa$). Equations (2–7) are the collected boundary value equations for the configuration depicted in Fig. 2. The parameters Γ_p, ξ, and α are, in general, complex-valued. This result is a consequence of the time phasing differences between the energy and momentum equations, and is accounted for by the polytropic model defined by Eq. (1).

III. Closed-Form Solution for Simple Tube Geometry

Equations (2–7) describe a boundary value problem that cannot be solved analytically in the most general form where temperature, fluid parameters, and geometry vary as a function of longitudinal position. However, if one assumes that the gas properties and tube radius remain constant as a function of x, Eq. (2) can be integrated to give

$$P(x,\omega) = A(\omega)e^{\omega\Gamma_p(x/c)} + B(\omega)e^{-\omega\Gamma_p(x/c)} \tag{8}$$

The upstream and downstream boundary conditions are used to solve for the constants of integration to give a closed-form *solution* valid for a straight tube with constant fluid properties.

$$P(x,\omega) = P_0(\omega)\frac{\cosh\{\omega\Gamma_p[(x-L)/c]\} - V(\omega\Gamma_p/A_c c)\sinh\{\omega\Gamma_p[(x-L)/c]\}}{\cosh[\omega\Gamma_p(L/c)] + V(\omega\Gamma_p/A_c c)\sinh[\omega\Gamma_p(L/c)]} \tag{9}$$

Evaluating Eq. (9) at $x = L$ gives the *end-to-end* frequency response of the configuration depicted in Fig. 2.

$$\frac{P_L(\omega)}{P_0(\omega)} = \frac{1}{\cosh[\omega\Gamma_p(L/c)] + V(\omega\Gamma_p/A_c c)\sinh[\omega\Gamma_p(L/c)]} \tag{10}$$

Collectively, Eqs. (9) and (10) are referred to as the *fundamental solution* and will be used to generate solutions to more complex serial and parallel configurations throughout the remainder of this report.

IV. Solution for a Cascaded Geometry

As discussed earlier, the (closed-form) fundamental solution is limited to applications where the temperature gradients are small, fluid properties are constant, and the tube radius is constant. However, by using Eqs. (9) and (10) as building blocks, solutions allowing longitudinal variation of the fluid properties and complex tube geometries can be constructed. The solution is recursive, and moves from the downstream boundary to the upstream boundary. The solution is performed assuming n solution elements that are not necessarily evenly spaced. The junction points between elements are referred to as *nodes*. Within each element the fluid properties are assumed to be constant, but the properties between nodes are allowed to vary. At each node, the equation of continuity is satisfied, giving a new downstream condition. To allow for a more general configuration, the tube diameter and cross section area are allowed to vary between each node. An entrapped volume that models tube fittings is allowed between each of the constant tubing sections. The entrapped volume is considered to have negligible length when compared to the length connecting sections of tubing. Two distinct approaches to solving the cascaded geometry problem are presented by Berg and Tijdeman [6], Tijdeman [7], Whitmore et al. [9,10], and Whitmore [11]. As the method of [9–11] will be used later to develop the general solution for branched (parallel) tube geometry; this method will be presented here for cascaded systems. Then parallel solution model will leverage the results of the cascaded system derivation to complete the derivation.

Consider a system with node n being the transducer node, and node $n-1$ being the adjacent upstream node. The schematic corresponding to this configuration is depicted in Fig. 3.

Across the control volume from node $n-1$ to node n, the system mass flow balance is

$$\rho_{n-1}U_{n-1}A_{c_{n-1}} = \frac{\partial\rho_{n-1}}{\partial t}V_{n-1} + A_{c_n}\frac{\partial}{\partial t}\int_{L_{n-1}}^{L_n}\rho(x)\,\mathrm{d}x + \frac{\partial\rho_n}{\partial t}V_n \tag{11}$$

In Eq. (11) the term on the left-hand side is the mass flow into node $n-1$. The first term on the right-hand side of Eq. (11) is the rate of change of mass at node $n-1$, the second term is the rate of change of mass within the tubing connecting node $n-1$ to node n, and the final term is the rate of change of mass at node n. The local density in Eq. (11) can be related to the pressure using the ideal gas law,

$$P = \rho R_g T = \frac{\rho c^2}{\gamma} \tag{12}$$

The time derivative of the local density in Eq. (11) is related to the rate of change of pressure by differentiating the polytropic expansion law with respect to time,

$$\frac{\partial P}{\partial t} = K\xi\frac{\rho^{\xi}}{\rho}\frac{\partial\rho}{\partial t} = \xi\frac{P}{\rho}\frac{\partial\rho}{\partial t} = \frac{\xi}{\gamma}c^2\frac{\partial\rho}{\partial t} \tag{13}$$

Substituting Eqs. (12) and (13) into Eq. (11), transforming to the frequency domain by letting

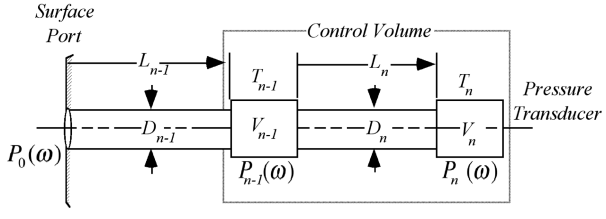

Fig. 3 Two node cascade geometry.

$$\frac{\partial}{\partial t}(\,) = \mathrm{j}\omega(\,)$$

and rearranging to solve for the mean velocity at $n-1$, Eq. (11) becomes

$$U_{n-1} = \frac{j\omega}{\rho_{n-1}}\left\{\frac{V_{n-1}}{A_{c_{n-1}}}\frac{P_{n-1}}{(\xi/\gamma)c_{n-1}^2} + \frac{A_{c_n}}{A_{c_{n-1}}}\int_{L_{n-1}}^{L_n}\left[\frac{P(x)}{(\xi/\gamma)c_{(x)}^2}(x)\right]\mathrm{d}x + \frac{V_n}{A_{c_n}}\frac{P_n}{(\xi/\gamma)c_n^2}\right\} \tag{14}$$

Assuming that $\rho_{n-1} \sim \rho_0$ (small flow velocities) the downstream boundary condition, Eq. (4), is used to eliminate U_{n-1} from Eq. (14), and the pressure gradient at node $n-1$ is written as

$$\frac{\mathrm{d}P(x,\omega)}{\mathrm{d}x} = \frac{V_{n-1}}{A_{c_{n-1}}}\left(\frac{\omega\Gamma_{p_{n-1}}}{c_{n-1}}\right)^2\left\{P_{n-1} + \frac{A_{c_n}}{V_{n-1}}\left(\frac{c_{n-1}}{c_n}\right)^2\int_{L_{n-1}}^{L_n}P(x)\,\mathrm{d}x + \frac{V_n}{V_{n-1}}\left(\frac{c_{n-1}}{c_n}\right)^2 P_n\right\} \tag{15}$$

The geometry from node $n-1$ to n is identical to the simple geometry depicted in Fig. 2; as a result the fundamental solution of Eq. (9) can be substituted into Eq. (15) and integrated. Additionally, the fundamental end-to-end frequency response, Eq. (10), can be used to write P_n in terms of P_{n-1}. Performing the integration, simplifying, and collecting terms, Eq. (15) reduces to

$$\left(\frac{\mathrm{d}P}{\mathrm{d}x}\right)_{n-1} = -\frac{Ve_{n-1}}{A_{c_{n-1}}}\left(\frac{\omega\Gamma_{p_{n-1}}}{c_{n-1}}\right)^2 P_{n-1} \tag{16}$$

In Eq. (16) Ve is the "*effective volume*," a parameter that accounts for the impedance of the downstream tube and volume as well as the volume at node $n-1$. In terms of the geometrical parameters, the effective volume is given by

$$Ve_{n-1} = V_{n-1}\left[1 + \frac{(c_{n-1}/c_n)^2(V_n/V_{n-1})\{\cosh[\omega\Gamma_{p_n}(L_n/c_n)] + [1/\omega(V_n/A_{c_n})(\Gamma_{p_n}/c_n)]\sinh[\omega\Gamma_{p_n}(L_n/c_n)]\}}{\cosh[\omega\Gamma_{p_n}(L_n/c_n)] + \omega(V_n/A_{c_n})(\Gamma_{p_n}/c_n)\sinh[\omega\Gamma_{p_n}(L_n/c_n)]}\right] \tag{17}$$

Because Ve is not a function of x, the form of Eq. (16) is identical the form of original boundary condition at node n, with Ve_{n-1} replacing V_n. Equation (16) can be applied as a new downstream boundary condition for a node $(n-2)$ upstream of node $n-1$. Repeating the procedure as described by Eqs. (11–17), the solution at node $n-2$ written directly as

$$P_{n-1}(\omega) = \frac{P_{n-2}(\omega)}{\cosh[\omega\Gamma_{p_{n-1}}(L_{n-1}/c_{n-1})] + \omega(Ve_{n-1}/A_{c_{n-1}})(\Gamma_{p_{n-1}}/c_{n-1})\sinh[\omega\Gamma_{p_{n-1}}(L_{n-1}/c_{n-1})]} \tag{18}$$

As described in detail in Whitmore et al. [9], the process is repeated n times and a general expression for the frequency response at each node is developed recursively by applying the solution at the previous node. The product of the frequency responses at each node gives the end-to-end frequency response.

$$\frac{P_L(\omega)}{P_0(\omega)} = \frac{P_1(\omega)}{P_0(\omega)}\frac{P_3(\omega)}{P_2(\omega)}\cdots\frac{P_{n-1}(\omega)}{P_{n-2}(\omega)}\frac{P_L(\omega)}{P_{n-1}(\omega)} = \prod_{i-1}^{n}\frac{1}{\cosh[\omega\Gamma_{p_i}(L_i/c_i)] + \omega(Ve_i/A_{c_i})(\Gamma_{p_i}/c_i)\sinh[\omega\Gamma_{p_i}(L_i/c_i)]} \tag{19}$$

In Eq. (19) the effective volume at node i is given by

$$Ve_i = V_i\left[1 + \frac{(c_i/c_{i+1})^2(Ve_{i+1}/V_1)(\cosh[\omega\Gamma_{p_{i+1}}(L_{i+1}/c_{i+1})] + [1/\omega(Ve_{i+1}/A_{c_{i+1}})(\Gamma_{p_{i+1}}/c_{i+1})]\{\sinh[\omega\Gamma_{p_{i+1}}(L_{i+1}/c_{i+1})]\})}{\cosh[\omega\Gamma_{p_{i+1}}(L_{i+1}/c_{i+1})] + \omega(Ve_{i+1}/A_{c_{i+1}})(\Gamma_{p_{i+1}}/c_{i+1})\sinh[\omega\Gamma_{p_{i+1}}(L_{i+1}/c_{i+1})]}\right] \tag{20}$$

At last node (n), $Ve_n = V_n$, i.e., the effective volume is simply the physical volume entrapped at the pressure transducer. In general the effective volume is a complex number and only the last node will have a real-valued volume.

The solution of Eq. (20) assumes that the tube diameter and temperature are prescribed at each node, and the fluid properties are evaluated as a function of the prescribed temperature. There is no restriction, however, for the prescribed diameter and temperature to be constant along the tube. Equations (19) and (20) allow a finite element solution of the original boundary value problem for an arbitrary cascaded geometry. Because boundary value equations have been analytically integrated at each element, no numerical integration is performed and this method is not subject to numerical stability problems that may be encountered with the finite difference methods. Changing the density of the finite element grid only changes the resolution of the solution. The grid density has no effect on the stability of the solution and a moderately coarse grid (less than 10 elements) generally produces acceptable results.

V. Solution for Parallel Sensor Geometry

The solution for a parallel geometry is an extension of the solution for the serial geometry and proceeds in a similar manner. Tubing from a surface port connects to a central or *main node* where two or more lines branch. A volume that can be taken to represent the entrapped volume of a pressure sensor terminates the end of each branch. This two-branch configuration is depicted in Fig. 4.

The *mass flow* balance at main node (V_m) is given by

$$\rho_m U_m A_{c_m} = \frac{\partial\rho_m}{\partial t}V_m + A_{c_{n-1}}\frac{\partial}{\partial t}\int_m^{L_{n-1}}\rho(x)\,\mathrm{d}x + \frac{\partial\rho_{n-1}}{\partial t}V_{n-1} + A_{c_n}\frac{\partial}{\partial t}\int_m^{L_n}\rho(x)\,\mathrm{d}x + \frac{\partial\rho_n}{\partial t}V_n \tag{21}$$

In Eq. (21) the term on the left-hand side is the mass flow into main node. The first term on the right-hand side of Eq. (21) is the rate of change of mass within the main node, the second term is the rate of change of mass within the tubing of branch $n-1$, the third term is the rate of change of mass at node $n-1$, the fourth term is the rate of change of mass within the tubing of branch n, and the final term is the rate of change of mass at node n. In a manner identical to the cascaded analysis, the polytropic law and the general gas are used to write the local density in terms of pressure, and the mass balance equation is written in the frequency domain as

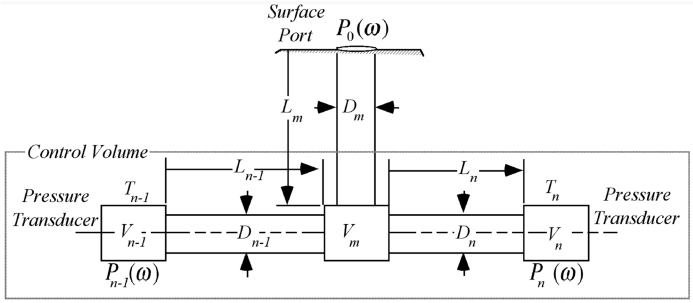

Fig. 4 Schematic of a two-branch sensor geometry.

$$U_m = \frac{j\omega}{\rho_m}\left\{\frac{V_m}{A_{c_m}}\frac{P_m}{(\xi/\gamma)c_m^2} + \frac{A_{c_n}}{A_{c_{n-1}}}\int_m^{L_{n-1}}\left[\frac{P(x)}{(\xi/\gamma)c_{(x)}^2}(x)\right]\mathrm{d}x + \frac{V_{n-1}}{A_{c_{n-1}}}\frac{P_{n-1}}{(\xi/\gamma)c_{n-1}^2}\right\} + \frac{j\omega}{\rho_m}\left\{\frac{A_{c_n}}{A_{c_{n-1}}}\int_m^{L_n}\left[\frac{P(x)}{(\xi/\gamma)c_{(x)}^2}(x)\right]\mathrm{d}x + \frac{V_n}{A_{c_n}}\frac{P_n}{(\xi/\gamma)c_n^2}\right\} \tag{22}$$

Using the downstream boundary condition, Eq. (4) to eliminate U_m from Eq. (22) yields the equation for the pressure gradient at the main node

$$\left(\frac{\mathrm{d}P}{\mathrm{d}x}\right)_m = -\frac{V_m}{A_{cm}}\left(\frac{\omega\Gamma_{p_m}}{c_m}\right)^2\left\{P_m + \frac{A_{c_{n-1}}}{V_m}\left(\frac{c_m}{c_{n-1}}\right)^2\int_m^{L_{n-1}}P(x)\,\mathrm{d}x + \frac{V_{n-1}}{V_m}\left(\frac{c_m}{c_{n-1}}\right)^2 P_{n-1}\right\} - \frac{V_m}{A_{c_0}}\left(\frac{\omega\Gamma_{p_m}}{c_m}\right)^2\left\{\frac{A_{c_n}}{V_m}\left(\frac{c_m}{c_n}\right)^2\int_m^{L_n}P(x)\,\mathrm{d}x + \frac{V_n}{V_m}\left(\frac{c_m}{c_n}\right)^2 P_n\right\} \tag{23}$$

As with the cascade analysis, the fundamental solution, Eq. (9), is used to evaluate the integrals in Eq. (23), and the end-to-end frequency response of the fundamental geometry, Eq. (10), is used to write P_{n-1} and P_n in terms of P_m. Performing the integrations, simplifying, and collecting terms, Eq. (23) reduces to

$$\left(\frac{\mathrm{d}P}{\mathrm{d}x}\right)_m = -\frac{Ve_m}{A_{c_m}}\left(\frac{\omega\Gamma_{p_m}}{c_m}\right)^2 P_m \tag{24}$$

Analogous to the cascaded solution, in Eq. (23), Ve is the "parallel effective volume," a parameter that accounts for the impedance of the tubes and volumes downstream of the main node. In general for n branches, the effective volume is given by the sum of the volume of the main node and the complex impedances of the individual branches

$$Ve_m = V_m\left[1 + \sum_{i=1}^{n}\Phi_i\right] \tag{25}$$

The parameter Φ_i in Eq. (25) is the complex impedance

$$\Phi_i = \left[\frac{(c_m/c_i)^2(V_i/V_m)\{\cosh[\omega\Gamma_{p_i}(L_i/c_i)] + [1/\omega(V_i/A_{c_i})(\Gamma_{p_i}/c_i)]\sinh[\omega\Gamma_{p_i}\frac{L_i}{c_i}]\}}{\cosh[\omega\Gamma_{p_i}(L_i/c_i)] + \omega(V_i/A_{c_i})(\Gamma_{p_i}/c_i)\sinh[\omega\Gamma_{p_i}(L_i/c_i)]}\right] \tag{26}$$

The form of Eq. (25) is identical to the form of the boundary condition for the fundamental solution. Based on this comparison, the solution for the frequency response at the main node relative to the input pressure is written by directly as

$$P_m(\omega) = \frac{P_0(\omega)}{\cosh[\omega\Gamma_{p_m}(L_m/c_m)] + \omega(Ve_m/A_{c_m})(\Gamma_{p_m}/c_m)\sinh[\omega\Gamma_{p_m}(L_m/c_m)]} \tag{27}$$

For each branch, the end-to-end frequency response is given by the complex product of the frequency response from the branch to the main node and the main node to the port (input pressure). For the jth branch, the end-to-end frequency response function is

$$\frac{P_j(\omega)}{P_0(\omega)} = \frac{1}{\{\cosh[\omega\Gamma_{p_m}(L_m/c_m)] + \omega(Ve_m/A_{c_m})(\Gamma_{p_m}/c_m)\sinh[\omega\Gamma_{p_m}(L_m/c_m)]\}\{\cosh[\omega\Gamma_{p_j}(L_j/c_j)] + \omega(Ve_j/A_{c_j})(\Gamma_{p_j}/c_j)\sinh[\omega\Gamma_{p_j}(L_j/c_j)]\}} \tag{28}$$

VI. Solution for Hybrid Geometries with Cascaded and Parallel Components

Using step-by-step application of the rules for cascade and parallel geometries presented in Eqs. (18–20) and (25–28), the frequency responses of pneumatic systems of arbitrary complexity can be analyzed. This process leads to an acoustical component reduction that is analogous to the

application of Kirchhoff's laws for complex electrical circuits [14]. Figure 5 illustrates this concept. Starting with the terminus of each branch, the branches are replaced with effective volumes until a single effective sensor response is obtained. The effective volumes at each point account for the collected complex impedances of the components downstream of that volume. Keeping track of the frequency response at each node allows the end-to-end frequency responses of each branch to be calculated. The reduction process will be illustrated using the configuration depicted in Fig. 5. The configuration depicted in Fig. 5 has two branches coming off of a main central junction. The first branch consists of a single line with a sensor at its terminus. The second branch is split into two additional branches.

The first step in the reduction process is to replace the second branch volume V_2 by its effective impedance Ve_2. The resulting effective volume is

$$Ve_2 = V_2\left[1 + \sum_{i=1}^{n} \frac{(c_2/c_{2i})^2(V_{2i}/V_2)\{\cosh[\omega\Gamma_{p_{2i}}(L_{2i}/c_{2i})] + [1/\omega(V_{2i}/A_{c2i})(\Gamma_{p_{2i}}/c_{2i})]\sinh[\omega\Gamma_{p_{2i}}(L_{2i}/c_{2i})]\}}{\cosh[\omega\Gamma_{p_{2i}}(L_{2i}/c_{2i})] + \omega(V_{2i}/A_{c2i})(\Gamma_{p_{2i}}/c_{2i})\sinh[\omega\Gamma_{p_{2i}}(L_{2i}/c_{2i})]}\right] \tag{29}$$

The frequency responses at the ends of the branches $\{2, 1\}$ and $\{2, 2\}$ with respect to the pressure at node $\{2\}$ are given by

$$\begin{bmatrix} \frac{P_{21}(\omega)}{P_2(\omega)} = \frac{1}{\{\cosh[\omega\Gamma_{p_2}(L_2/c_2)]+\omega(Ve_2/A_{c2})(\Gamma_{p_2}/c_2)\sinh[\omega\Gamma_{p_2}(L_2/c_2)]\}\{\cosh[\omega\Gamma_{p_{21}}(L_{21}/c_{21})]+\omega(Ve_{21}/A_{c21})(\Gamma_{p_{21}}/c_{21})\sinh[\omega\Gamma_{p_{21}}(L_{21}/c_{21})]\}} \\ \frac{P_{22}(\omega)}{P_2(\omega)} = \frac{1}{\{\cosh[\omega\Gamma_{p_2}(L_2/c_2)]+\omega(Ve_2/A_{c2})(\Gamma_{p_2}/c_2)\sinh[\omega\Gamma_{p_2}(L_2/c_2)]\}\{\cosh[\omega\Gamma_{p_{22}}(L_{22}/c_{22})]+\omega(Ve_{22}/A_{c22})(\Gamma_{p_{22}}/c_{22})\sinh[\omega\Gamma_{p_{22}}(L_{22}/c_{22})]\}} \end{bmatrix} \tag{30}$$

Replacing the physical at node $\{2\}$ by the effective volume (Ve_2), Fig. 5 can be redrawn as shown in Fig. 6.

The analysis procedure on the reduced configuration now becomes identical to the parallel procedure described in the preceding section except that Ve_2 replaces V_2 in the index bookkeeping. When the analysis is completed the end-to-end frequency response of the branches $\{2, 1\}$ and $\{2, 2\}$ is given by Eq. (31), where $i = \{1, 2\}$:

$$\frac{P_{2i}(\omega)}{P_0(\omega)} = \frac{P_{2i}(\omega)}{P_2(\omega)}\frac{P_2(\omega)}{P_0(\omega)} = \frac{1}{\{\cosh[\omega\Gamma_{p_m}(L_m/c_m)] + \omega(Ve_m/A_{c_m})(\Gamma_{p_m}/c_m)\sinh[\omega\Gamma_{p_m}(L_m/c_m)]\}} \times \frac{1}{\{\cosh[\omega\Gamma_{p_2}(L_2/c_2)] + \omega(Ve_2/A_{c_2})(\Gamma_{p_2}/c_2)\sinh[\omega\Gamma_{p_2}(L_2/c_2)]\}\{\cosh[\omega\Gamma_{p_{2i}}(L_{2i}/c_{2i})] + \omega(Ve_{2i}/A_{c_{2i}})(\Gamma_{p_{2i}}/c_{2i})\sinh[\omega\Gamma_{p_{2i}}(L_{2i}/c_{2i})]\}} \tag{31}$$

VII. Experimental Validation Frequency Response Model for Branched Configurations

The serial frequency response model has been thoroughly validated by the authors of [6,7,9–11]. This section will emphasize the presentation of experimental data to verify the computations of the parallel frequency response model presented in the preceding sections. Figure 7 illustrates the experimental apparatus used to generate the data.

In this experiment frequency response measurements were gathered using a test plate mounted at the end of an insulated cylindrical sound chamber. A piezoelectric microphone was flush mounted on the test plate and measured the reference sound pressure. The pneumatic configuration consisted of a surface port on the plate and a section of branched tubing. Microphones identical to the reference microphone measured the response at the end of each tubing branch. For each test the layout, the geometric parameters including tubing lengths, internal diameters, and volumes were carefully measured and recorded as inputs for comparison with analytical calculations. Ambient temperature and barometric pressure measurements were recorded at the beginning of each test using a hand help barometer and laboratory thermometer. The barometric data were used to calculate the mean density and viscosity.

For these tests, a broadband waveform was generated by a microcomputer outfitted with a 12-bit digital-to-analog (D/A) conversion board and was amplified using commercial high-fidelity stereo equipment. The waveform was used to excite a large subwoofer-class stereo speaker inserted in the sealed test chamber. Speaker volume was controlled using a voltage attenuator on the signal output from a microcomputer control board. The broadband waveform used to excite the speaker was generated by a nonlinear phase modulated cosine wave of the form

$$S(t) = \sum_{i=1}^{N_h} \cos\left[[2\pi f_0 + (i)\delta f]t + \frac{i^3\pi}{N_h}\right] \tag{32}$$

In Eq. (32), N_h is the number of harmonics desired in the output signal, f_0 is the fundamental frequency, δf is the frequency increment between harmonics, and t is the time from the beginning of the waveform. Figure 8 shows a typical waveform and the resulting spectral magnitude plot. The waveform of Eq. (32) was chosen to generate a very flat spectrum that also limited amplitude envelope in the time domain. That is, no large voltage "spike" is required to generate the flat spectrum as is required when a linearly phase modulated wave is used.

Evaluating the Fourier transforms of the reference and test microphones and taking the complex ratio resulting spectra evaluated the frequency response for each branch. Output signals from the reference and test microphones were amplified and sampled at 24 kHz by a 16-bit analog-to-digital (A/D) conversion board in the microcomputer. Direct current (dc) offsets in the microphone outputs were removed by alternating current (ac) coupling the microphone outputs to give a minimum sensible frequency of 2.5 Hz. The flat frequency responses of the microphones and signal conditioning extended to well beyond 2000 Hz. At midrange output levels from the D/A converter (2.5 V), the amplified sound pressure level (SPL) in the chamber was 145 dB (0.36 kPa psf). This SPL is well within the linear response regions of the reference and test microphones. In the linear range these microphones have an unamplified response sensitivity of 10.4 V/psf. Using amplifier gains settings of 10 and a full-scale A/D range of ± 1 V, the nominal resolution of the microphone least significant bit (lsb) was 0.138 Pa/lsb.

VIII. Comparison of Frequency Response Data to Analytical Solutions

Several pneumatic configurations were tested. These geometries included balanced geometries with identical impedances on each side of the main node, and unbalanced geometries with different impedances on each side of the main node. The comparisons between the laboratory data

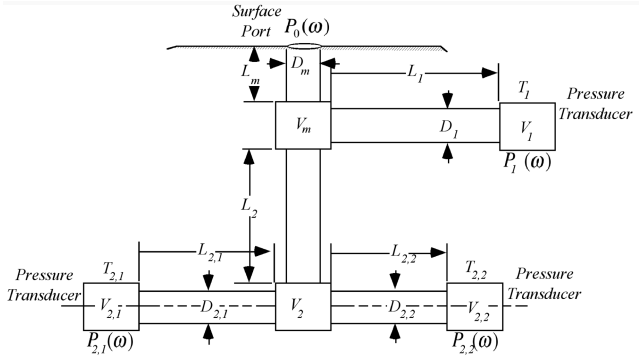

Fig. 5 Example of reduction process for analysis of complex pneumatic layouts.

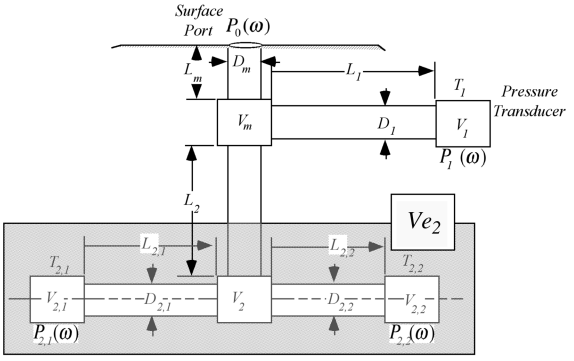

Fig. 6 Hybrid configuration with branch replaced by effective impedance.

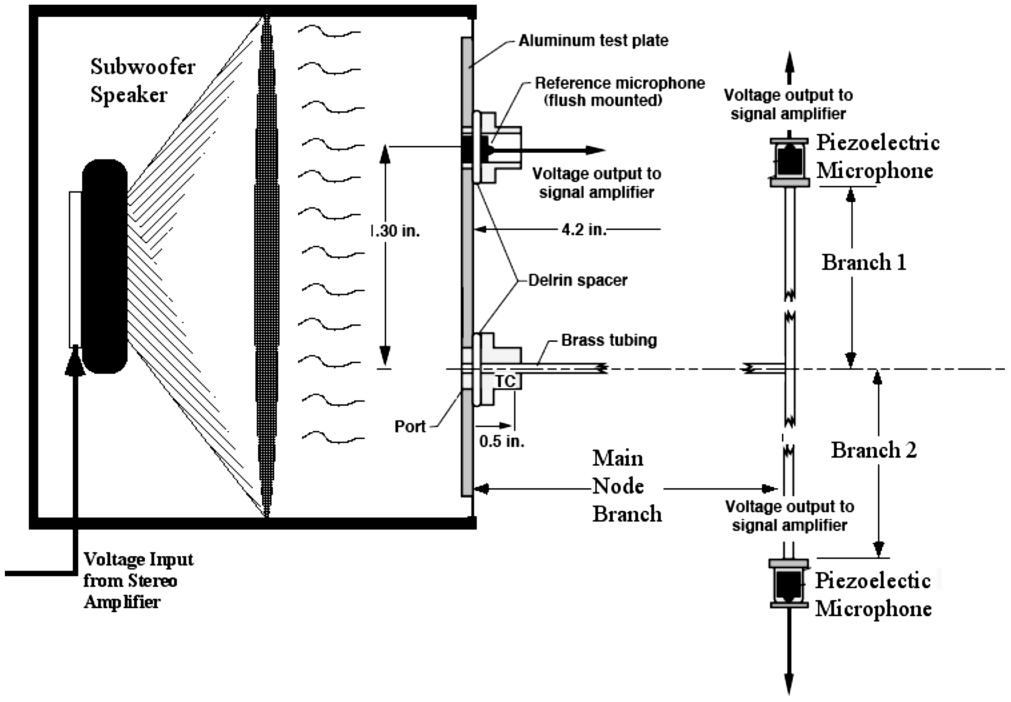

Fig. 7 Apparatus used for frequency response tests.

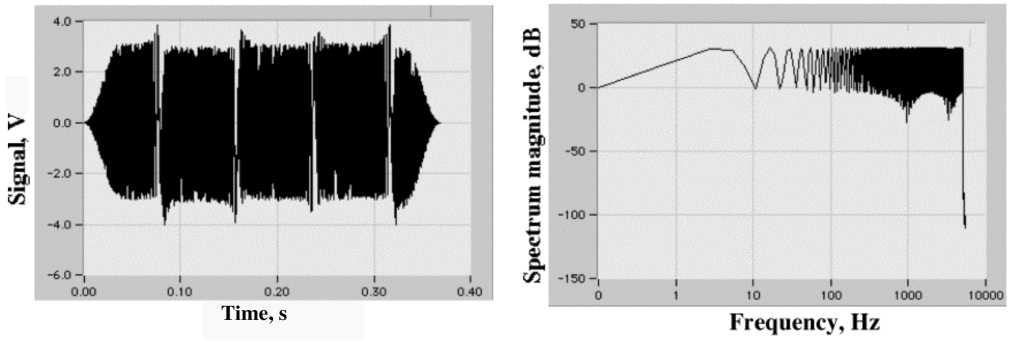

a) Excitation wave form **b) Wave form spectrum**

Fig. 8 Phase modulated waveform used for frequency response tests.

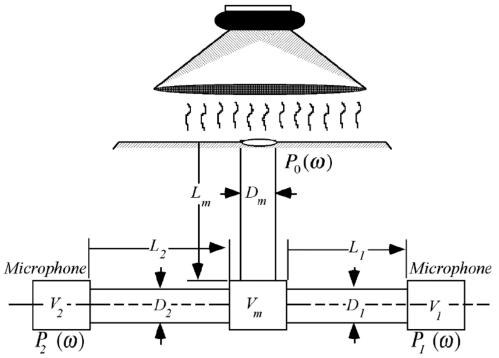

Fig. 9 Schematic of test configuration.

and the calculations were excellent for all cases and the balance between branch impedances was not a factor in the quality of the comparisons. A schematic of the test geometry is presented in Fig. 9. Table 1 summarizes the test configurations.

Figure 10 compares the sensed and calculated frequency response for a balanced configuration where both branches have identical layouts. In this configuration, the length of tubing (L_m) from the input port to the main node is 12 in. (30.48 cm). The tubing length (L_1) from the main node to the terminus of the first branch is 10 in. (25.4 cm). The tubing length (L_2) from the main node to the end of the second branch is also 10 in. (25.4 cm). In all cases the internal diameter (D) of the tubing is 0.115 in. (0.045 cm). The entrapped volume at the main node (V_m) is 0.001 in.^{3} (0.0164 cm^3). The entrapped volume within the microphone housings at the end of each branch (V_1, V_2) is 0.0025 in.^{3} (0.0328 cm^3). Figure 11 compares the sensed and calculated frequency response for an unbalanced configuration where L_2 is lengthened from 10 in. (25.4 cm) to 15 in. (38.1 cm) All other aspects of the geometry are identical to the case presented in Fig. 10.

Figure 10a displays the magnitude plot of the first branch with the ordinate showing the response magnitude ratio in decibels and the abscissa showing the log of the input frequency in hertz. The solid line is the calculated magnitude ratio and the open symbols are the laboratory data. Also plotted for contrast is the calculated magnitude ratio of the first branch if the impedance of the second branch is ignored. Figure 10b shows the phase angle plot. The model accounts for the effect of branch 2 on branch 1, and the magnitude attenuation and additional phase delay due to the extra impedance is clearly identified. A single-branch model of this configuration would be very inaccurate. The second branch frequency response is nearly identical and is not shown here.

Figures 11a and 11b plot the magnitude and phase comparisons for the unbalanced configuration branch 1, and Figs. 11c and 11d plot the magnitude and phase comparisons for the unbalanced configuration branch 2.

Again the comparisons between the calculated and measured frequency responses are excellent. The reflected waves between the two branches superimposed on the main harmonics are clearly identifiable. The comparisons presented in Figs. 10 and 11 are typical of results obtained from this series of experiments.

IX. Conclusions

Modern airdata systems can have complex pneumatic layouts with multiple branches connecting pressure sources to instruments, cockpit displays, or other avionics components. These branches will induce significant attenuation and latency in the system measurements. This paper has developed a model that calculates the frequency response of branched pneumatics systems. The frequency response model presented has not been previously published in open literature. The model predictions are compared against data generated by a series of laboratory experiments. Two typical experimental cases are presented. The comparisons are very favorable and provide empirical validation of the model predictions. Using step-by-step application of the rules presented for cascaded and parallel geometries, the frequency responses of pneumatic systems of arbitrary complexity can be analyzed. The resulting process is analogous to Kirchhoff's laws used to analyze complex

Table 1 Summary of the test configurations

Configuration	Main node			Branch 1			Branch 2		
	V_m, in.^{3}	D_m, in.	L_m, in.	V_1, in.^{3}	D_1, in.	L_1, in.	V_2, in.^{3}	D_2, in.	L_2, in.
Balanced	0.001	0.115	12.0	0.0025	0.115	10.0	0.0025	0.115	10.0
Unbalanced	0.0001	0.115	12.0	0.0025	0.115	10.0	0.0025	0.115	15.0

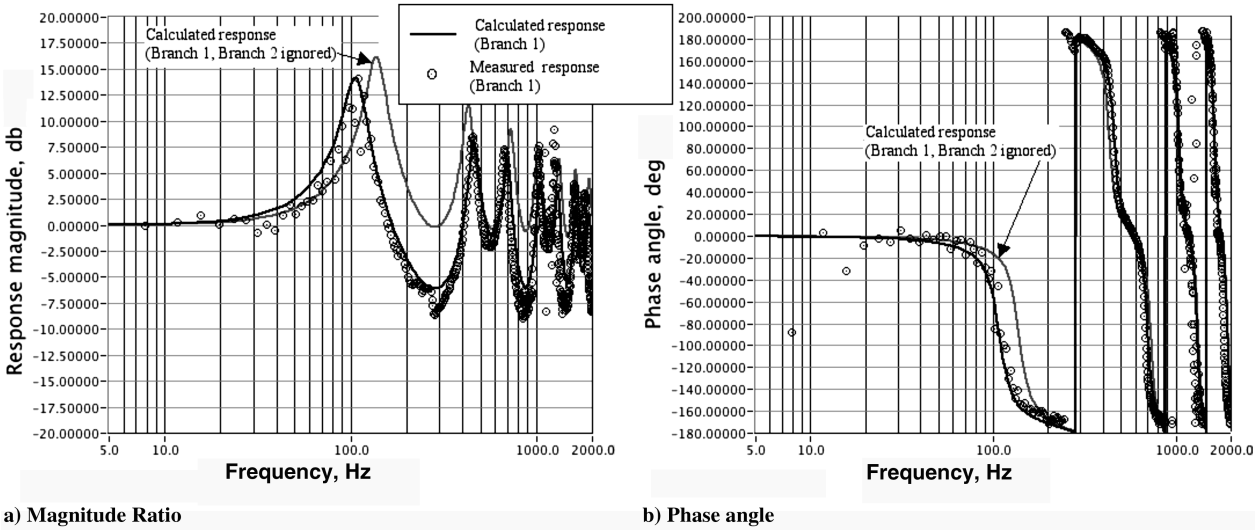

a) Magnitude Ratio **b) Phase angle**

Fig. 10 Comparison of calculated and measured frequency response with balanced branch impedances.

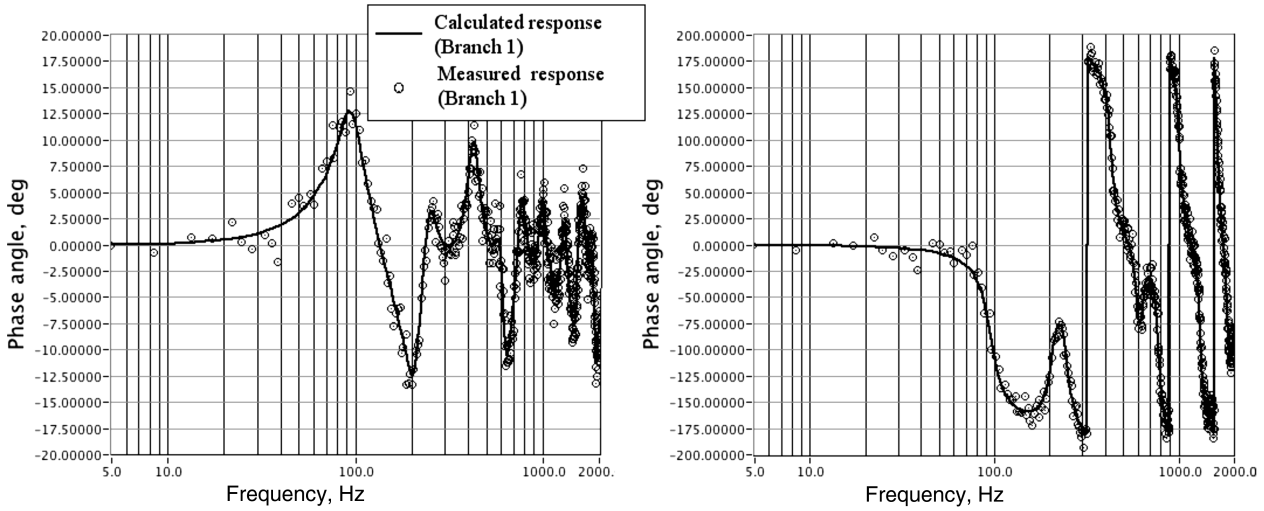

a) Branch 1 magnitude ratio

b) Branch 1 phase angle

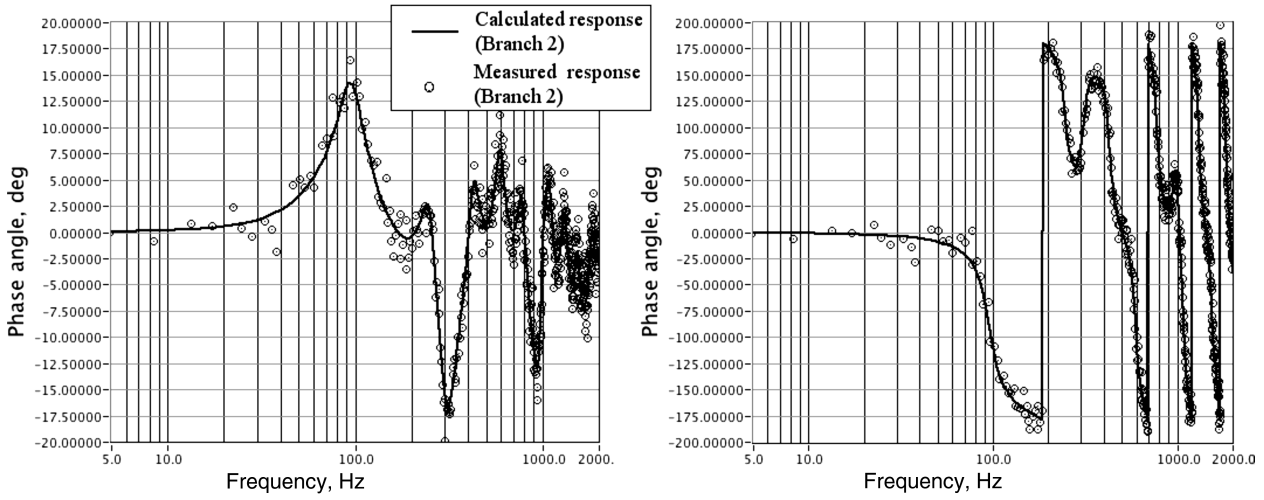

c) Branch 2 magnitude ratio

d) Branch 2 phase angle

Fig. 11 Comparison of calculated and measured frequency response with unbalanced branch impedances.

electrical circuits. The model allows instrumentation designers to evaluate the responses of arbitrarily complex pneumatic systems over a wide range of flow conditions in a general and unified way. Using this model potential fidelity problems can be identified and resolved before pneumatic components are installed. By applying this method to an installed aircraft system, the calculated transfer functions can be used for real-time attenuation and latency compensation using previously published spectral deconvolution methods.

References

[1] Stephens, R. W. B., and Bate, A. E., *Acoustics and Vibrational Physics*, St. Martin Press, New York, 1966, pp. 203–266.

[2] Iberall, A. S., "Attenuation of Oscillatory Pressures in Instrument Lines," U.S. National Bureau of Standards NBS-RP 2115, Vol. 45, Washington, DC, Jan. 1950.

[3] Lamb, R. C., "The Influence of Geometry Parameters Upon Lag Error in Airborne Pressure Measurement Systems," Wright Air Development Center WADC-TR 57-351, Wright–Patterson AFB, Ohio, July 1957.

[4] Schuder, C. B., and Binder, R. C., "The Response of Pneumatic Transmission Lines to Step Inputs," *Journal of Basic Engineering*, Vol. 81, No. 12, 1959, pp. 578–584.

[5] Hougen, J. O., Martin, O. R., and Walsh, R. A., "Dynamics of Pneumatic Transmission Lines," *Control Engineering*, Vol. 10, No. 3, March 1963, pp. 114–117.

[6] Berg, H., and Tijdeman, H., "Theoretical and Experimental Results for the Dynamic Response of Pressure Measuring Systems," Nat. Luchtavaatlab NLR-TR F.238, Amsterdam, Jan. 1965.

[7] Tijdeman, H., "Investigation of the Transonic Flow Around Oscillating Airfoils," Nat. Luchtavaatlab NLR-TR 77090 U, Amsterdam, 1977.

[8] Parrot, T., and Zorumski, W., "Sound Transmission Through a High-Temperature Acoustic Probe Tube," *AIAA Journal*, Vol. 30, No. 2, 1992, pp. 318–323.

[9] Whitmore, S. A., Petersen, B. J., and Scott, D. D., "A Dynamic Response Model for Pressure Sensors in Continuum and High Knudsen Number Flows with Large Temperature Gradients," NASA TM-4728, Jan. 1996.

[10] Whitmore, S. A., and Petersen, B. J., "Dynamic Response of Pressure Sensing Systems in Slip-Flow with Temperature Gradients," *AIAA Journal*, Vol. 37, No. 6, 1999, pp. 772–774.

[11] Whitmore, S. A., "Frequency Response of Pressure Sensor Configurations in Slip-Flow Conditions," *Journal of Spacecraft and Rockets*, Vol. 39, No. 2, March–April 2002, pp. 219–226.

[12] Whitmore, S. A., and Leondes, C. T., "Pneumatic Distortion Compensation for Aircraft Surface Pressure Sensing Devices," *Journal of Aircraft*, Vol. 28, No. 12, Dec. 1991, pp. 828–836.

[13] Doebelin, E. O., *Measurement Systems, Application and Design*, McGraw–Hill, New York, 1983, pp. 404–456.

[14] Friedberger, W. F. (ed.), "Kircchoff Law," *International Dictionary of Applied Mathematics*, D. Van Nostrand & Company, Inc., Princeton, NJ, 1960, pp. 512–513.